JOURNAL OF PROPULSION AND POWER
Vol. 10, No. 5, Sept.–Oct. 1994

Study of the Compressible Flow in a Diffusing S-Duct

Steven R. Wellborn*
Iowa State University, Ames, Iowa 50011
Bruce A. Reichert†
NASA Lewis Research Center, Cleveland, Ohio 44135
and
Theodore H. Okiishi‡
Iowa State University, Ames, Iowa 50011

Benchmark aerodynamic data are presented for compressible flow through a representative S-duct configuration. Measurements of the three-dimensional velocity field, total pressures, and static pressures were obtained in five cross-sectional planes. Surface static pressure and surface flow visualization data were also acquired. All reported tests were conducted with an inlet centerline Mach number of 0.6. The Reynolds number, based on the inlet centerline velocity and duct inlet diameter, was 2.6×10^6. Thin inlet turbulent boundary layers existed. The collected data should be beneficial to aircraft inlet designers and are suitable for the validation of computational codes. The results show that a region of streamwise flow separation occurred within the duct. Measurements indicate that the duct curvature induced strong pressure-driven secondary flows. The crossflows evolved into counter-rotating vortices. These vortices convected low momentum fluid of the boundary layer toward the center of the duct, degrading both the uniformity and magnitude of the total pressure profile.

Nomenclature

A	=	duct cross-sectional area perpendicular to the centerline
Cp	=	static pressure coefficient, $p - p_{cl}/p_{0,cl} - p_{cl}$
Cp_0	=	total pressure coefficient, $p_0 - p_{cl}/p_{0,cl} - p_{cl}$
d	=	duct diameter
H	=	shape factor, δ^*/θ
M	=	normalized local Mach vector, M/M_{cl}
p	=	static pressure
p_0	=	total pressure
R	=	centerline circular arc radius
r	=	duct radius
s	=	arc length along the duct centerline
x, y, z	=	duct Cartesian coordinates
δ	=	inlet boundary-layer thickness
δ^*	=	inlet displacement thickness
Θ	=	streamwise centerline arc angle
θ	=	inlet momentum thickness
ϕ	=	cross-stream polar angle

Subscripts

cl	=	centerline position
1, 2	=	stations before and after the S-duct

Introduction

AIRCRAFT propulsion systems often use S-ducts. A primary purpose of an S-duct is to convey airflow from the wing or fuselage intake to the engine compressor. Compressible, subsonic inlet flow conditions usually exist for this application. A secondary purpose of an S-duct is to conceal the compressor face and provide a multiple bounce cavity for radar deflection. Examples of commercial aircraft with S-ducts include the Boeing 727 and Lockheed Tristar L-1011. Military aircraft—the General Dynamics F-16, McDonnell Douglas F-18, and the Lockheed YF-22—use S-shaped ducts.

Diffusing S-ducts have centerline curvature and a cross-sectional area increase. Curvature of the centerline or changes in the duct cross-sectional shape give rise to streamline curvature. Cross-stream pressure gradients, resulting from streamline curvature, can produce significant secondary flows. These secondary flows convect boundary-layer fluid from the duct surface to the center of the duct, creating nonuniform cross-stream total pressure profiles. Additionally, the adverse streamwise pressure gradient, caused by increasing cross-sectional area, can lead to flow separation.

Well-designed diffusing S-ducts should efficiently decelerate the incoming flow without the occurrence of streamwise separation. Moreover, to achieve appropriate engine performance, the diffusing S-duct must also incur minimal total pressure losses and deliver nearly uniform flow with small transverse velocity components at the engine compressor entrance. An aircraft engine inlet designer often faces a difficult dilemma. Size and weight restrictions usually encourage the use of shorter S-ducts. Shorter ducts result in greater streamline curvature and larger adverse pressure gradients, which in turn produce substantial secondary flows, nonuniform total pressure distributions, and possible flow separation. Any of these flow attributes can result in unacceptable duct performance.

The design and implementation of earlier S-duct components relied heavily on test-stand data. The development of the Boeing 727 center engine inlet[1] and the examination of scoop diffusers used in conjunction with high-speed turboprop-fan engines[2] exemplify this trend. To aid in design, experimental studies have also been performed on S-ducts which represent simplified models of engine inlets.[3–8] These studies were conducted to qualitatively examine S-duct flowfields and provide better understanding of the fluid mechanics. These studies discovered that counter-rotating vortices formed within most S-ducts. Rowe[3] concluded that the development of the

Presented as Paper 92-3622 at the AIAA/SAE/ASME/ASEE 28th Joint Propulsion Conference and Exhibit, Nashville, TN, July 6–8, 1992; received July 26, 1993; revision received Dec. 17, 1993; accepted for publication Jan. 26, 1994. Copyright © 1994 by the American Institute of Aeronautics and Astronautics, Inc. No copyright is asserted in the United States under Title 17, U.S. Code. The U.S. Government has a royalty-free license to exercise all rights under the copyright claimed herein for Governmental purposes. All other rights are reserved by the copyright owner.

*Research Assistant, Mechanical Engineering Department. Student Member AIAA.

†Aerospace Engineer, Inlet, Duct, and Nozzle Flow Physics Branch, 21000 Brookpark Road. Member AIAA.

‡Professor and Chair, Mechanical Engineering Department. Member AIAA.

vortices was caused by strong pressure gradients, created by the streamline curvature, which acted on the low-momentum, boundary-layer fluid. Taylor et al.[7,9,10] found that the vortices were present in ducts having either circular or square cross sections. Guo et al.[6] noted that counter-rotating vortices were absent in S-ducts having large incident inlet flow angles, and instead, the entire exit flow rotated about the centerline.

Unfortunately, the majority of the studies involving simplified duct models were conducted with incompressible flow and/or thick boundary layers. Furthermore, only a few involved diffusing ducts. Most of the studies did not have streamwise separated flow, since the ducts were nondiffusing and/or had only mild centerline curvature. Streamwise separated flow did occur in the ducts studied by Bansod and Bradshaw.[4] However, the region of separation was small and had no significant effect on the flowfield. A large region of separated flow was present in a study by Sullivan et al.,[11] but only surface-flow visualization and surface-static pressure data were obtained. The only measurements of compressible flow through a diffusing S-duct experiencing separated flow were acquired by Vakili et al.[8] Further studies involving representative diffusing S-ducts, having streamwise separation, compressible inlet flow conditions, and thin turbulent inlet boundary layers, are needed to help interpret the fluid mechanics associated with S-ducts used for aeronautical applications.

The ability to predict the complicated three-dimensional flow phenomena associated with S-ducts without extensive experimental testing is obviously desirable for designers. Because of this, considerable computational effort has been focused on compressible flows through S-ducts. Researchers have recently turned their attention to complete Navier-Stokes analyses,[12-14] following much effort using reduced Navier-Stokes models.[15-18] These studies also suggest the formation of counter-rotating vortices within an S-duct. Streamwise flow separation was a dominant feature for S-ducts with large centerline displacements and/or cross-sectional area increases. A review of literature suggests that benchmark data exist for the validation of computational fluid dynamics codes applied to incompressible flow with thick inlet boundary layers through S-ducts.[6,7,9,10] However, only a limited amount of benchmark data exists for compressible S-duct flows with thin inlet boundary layers.[17] Further benchmark data detailing representative diffusing S-duct flows are needed for the validation of computational fluid dynamics codes.

The objective of this study was therefore twofold; first, to provide a comprehensive benchmark data set for the flow through a representative diffusing S-duct, and second, to reexamine and describe the complex fluid mechanics associated with diffusing S-duct flows having streamwise separation and applicable inlet flow characteristics. The experimental data were acquired along with a concurrent computational effort, with considerable beneficial synergism resulting from the combination. This concurrent approach also proved to be successful in a recent study of circular-to-rectangular transition duct flows.[19,20]

Experimental Facility

Detailed aerodynamic data for the flow through a circular cross section diffusing S-duct were acquired using the NASA Lewis Research Center Internal Fluid Mechanics Facility. This facility was designed to support tests of a variety of internal flow configurations. Complete details of the facility are described by Porro et al.[21] For this experiment, atmospheric test cell air was drawn through a large settling chamber, passed through the test section, and dumped into a large exhaust plenum. A diagram of the experimental facility is shown in Fig. 1.

The settling chamber conditioned the incoming flow with a series of wires, meshes, and screens. Air was drawn into the chamber through a large bell-mouth opening. A perforated spreader cone mixed the inlet flow. A coarse-mesh conditioning screen reduced mean flow nonuniformities. A honeycomb-screen combination removed large-scale turbulence fluctuations. A seamless contraction section uniformly accelerated the flow from the settling chamber. An area contraction ratio of 59 to 1 ensured a nearly uniform and low turbulence intensity flow at the test section entrance.

The test section for this experiment consisted of the diffusing S-duct and two constant area duct extensions. The first extension (10.21-cm diam) served as the interface between the contraction exit and the S-duct entrance. The second extension (12.57-cm diam) conveyed the flow from the S-duct to the exhaust region. The second extension was able to rotate about its centerline when the facility was shut down. Each extension was 76.2 cm long and had the same internal surface finish as the S-duct. Specific S-duct details are reviewed in the next section of this article.

The exhaust section contained a circular cross-section pipe, a mass-flow plug, and a subatmospheric plenum. The pipe was 244 cm long and had a diameter of 12.70 cm. The pipe housed the adjustable mass flow plug. The mass flow plug controlled the airflow through the entire facility. Mach numbers up to 0.95 within the test section were possible with this arrangement. Furthermore, the flow was always choked at the mass flow plug. Consequently, small variations of the exhaust vacuum pressure were isolated from the test flowfield. Flow was simply dumped into the subatmospheric pressure exhaust plenum, which had a 121.92-cm diam.

Diffusing S-Duct Geometry

The diffusing S-duct was intentionally designed to incorporate as many of the complex three-dimensional flow features, including the possibility of unsteady streamwise separation, which are associated with similar aircraft configurations. A half-shell representation of the diffusing S-duct is shown in Fig. 2. The duct centerline was defined by two planar circular arcs with identical radii R of 102.1 cm and subtended angles of 30 deg. The centerline coordinates, given by Eq. (1), are indicated by the dashed line in Fig. 2. All cross sections perpendicular to the centerline were circular. The duct inlet radius r_1 was 10.21 cm. The duct exit radius r_2 was 12.57

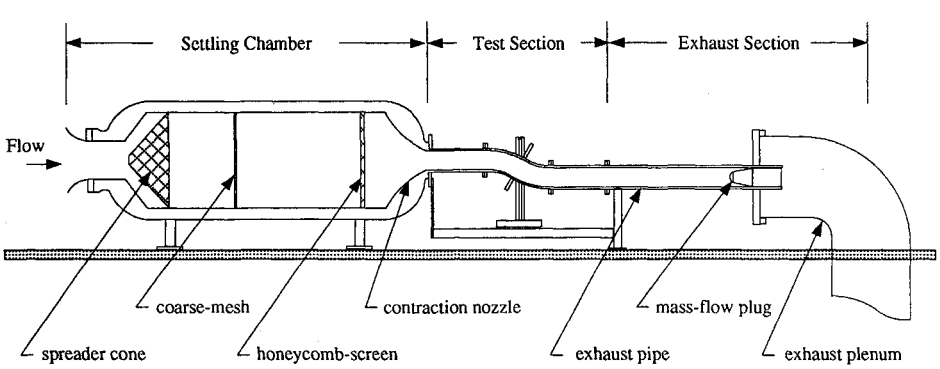

Fig. 1 Diagram of the internal fluid mechanics facility.

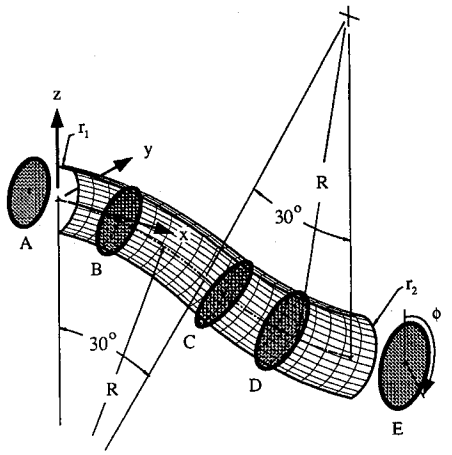

Fig. 2 Half shell drawing of the circular diffusing S-duct.

cm. This produced an area ratio A_2/A_1 of 1.52. The variation of the duct radius as a function of the centerline arc angle Θ (0 deg $\leq \Theta \leq$ 60 deg) is given by Eq. (2). The duct was larger than, but geometrically similar to, the duct tested by Vakili et al.[8]

For 0 deg $\leq \Theta \leq$ 30 deg

$$x_{cl} = R \sin \Theta$$

$$y_{cl} = 0$$

$$z_{cl} = R \cos \Theta - R$$

For 30 deg $\leq \Theta \leq$ 60 deg

$$x_{cl} = 2R \sin 30 \text{ deg} - R \sin(60 \text{ deg} - \Theta)$$

$$y_{cl} = 0$$

$$z_{cl} = 2R \cos 30 \text{ deg} - R - R \cos(60 \text{ deg} - \Theta) \quad (1)$$

$$\frac{r}{r_1} = 1 + 3\left(\frac{r_2}{r_1} - 1\right)\left(\frac{\Theta}{60 \text{ deg}}\right)^2 - 2\left(\frac{r_2}{r_1} - 1\right)\left(\frac{\Theta}{60 \text{ deg}}\right)^3 \quad (2)$$

The duct was milled from two separate blocks of aluminum and had a final tolerance of ± 0.0127 cm. After milling, the two halves were mated together and sanded using 120-grit Emory cloth until all machining imperfections were removed. The surface was then polished. The interior split line, located on the vertical centerline plane, was flush to touch and invisible to sight.

When discussing results, the S-duct is fixed to the coordinate system shown in Fig. 2. Axial position refers to the distance to cross-stream planes, normalized by the inlet diameter, measured along the duct centerline, beginning at the start of curvature. Positions within cross-stream planes are specified by ϕ, measured from the positive z axis, and the radial distance r measured from the centerline.

Instrumentation and Measurement Techniques

The flowfield was investigated with several different techniques. Flow visualization and wall static pressures were obtained on the S-duct surface. Calibrated three- and five-hole pneumatic probes were used to determine total pressures, static pressures, and the velocity field. Each measurement technique is briefly explained within this section.

The characteristics of the near surface flow were visualized by applying fluorescent oil to the surface. For this technique, a powder fluorescent dye (Rocket Red: Day-Glow Color Corporation) was mixed with 140-wt oil (STP), thinned with 5-wt oil and then applied to the surface in small dots. Surface streakline patterns developed while air was drawn through the duct. The patterns corresponded to surface flow direction and shear intensity. The duration of the test, at the desired flow rate, was 10 min. Following rapid shutdown, the duct was disassembled in order to observe the streaklines under the illumination of uv light. The patterns were photographed with a 35-mm camera using 400 ASA color film. An uv filter was used to reduce the glare produced by the reflection of the uv light from the duct surface. Permanent and temporary locating marks on the duct surface were used to permit quantitative use of the flow visualization data.

The flowfield was measured with calibrated three- and five-hole probes. Data were accumulated in five measurement planes, each perpendicular to the duct centerline. The measurement plane locations along the duct centerline are presented in Table 1. These planes are also depicted by the shaded cross sections in Fig. 2. The number of radial traverses and total measurements made in each plane are given in Table 1. Traversing intervals in the radial direction were approximately 0.254 cm for all measurement planes. In planes A and E, traversing intervals near the surface were 0.0635 cm. Reported flow measurements were concentrated in only one symmetric half of the duct. The aerodynamic data represent an arithmetic average of a number of measurements.

A calibrated three-hole probe was used in plane A, since a nearly one-directional velocity field existed there. The three-hole probe allowed total pressure, static pressure, and two components of velocity to be measured. A yaw-nulling measurement method was utilized. The maximum uncertainty of the total and static pressures measured by the three-hole probe were $\delta p_0 = \pm 0.0345$ kPa and $\delta p = \pm 0.0676$ kPa. This was determined by a propagation of error uncertainty analysis. The error in the yaw angle was due solely to the uncertainty of the actuator position which was ± 0.1 deg.

A calibrated five-hole probe was used in planes B, C, D, and E, enabling total pressure, static pressure, and three components of velocity to be measured. Both yaw-nulling and nonyaw-nulling measurement methods were employed. The calibration methods and data reduction procedures are not presented here, but are reviewed in detail in Refs. 22 and 23. A detailed uncertainty analysis of the errors associated with five-hole probe measurements is given by Reichert and Wendt.[24] From this analysis it was determined that the errors in total pressure, static pressure, and flow angles were strongly dependent on the measured local flow angle, with large errors corresponding with large measured flow angles. Most flow angles in the S-duct were under 20 deg. This leads to maximum uncertainties in total and static pressure of $\delta p_0 = \pm 0.0414$ kPa and $\delta p = \pm 0.0552$ kPa. The maximum uncertainty in flow angle was ± 0.17 deg.

A total of 209 static pressure taps were located on the surface of the duct. The taps were constructed by locally drilling a 0.143-cm-diam hole normal to the duct surface. Each hole was plugged with an appropriate-size aluminium tube having an i.d. of 0.0813 cm. Epoxy placed on the outside of the duct sealed the interface between duct and tube. The tube was sanded flush with the inside duct surface. The static taps were distributed in the streamwise and circumferential directions. Three lines of taps ran in the streamwise direction. These streamwise lines were at constant circumferential angles of ϕ = 10, 90, and 170 deg. Measurements at ϕ = 0 and 180 deg were impossible because of the flanges there. The streamwise taps were positioned every $s/d_1 = 0.0873$, beginning at $s/d_1 = 0.3492$. A total of 53 taps were in each stream-

Table 1 Measurement plane information

Plane	A	B	C	D	E
s/d_1	−0.50	0.96	2.97	4.01	5.73
Radial traverses	10	11	11	11	19
Measurements	590	462	506	539	930

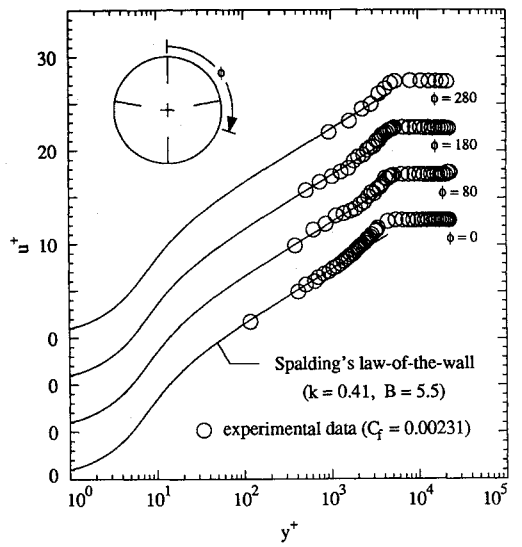

Fig. 3 Law-of-the-wall velocity profiles at four inlet circumferential locations.

wise line. Four lines of taps ran in the circumferential direction. These circumferential taps were in planes A, B, C, and D. Plane E was void of static taps. The circumferential static taps were spaced 20 deg in plane A, and 10 deg in planes B, C, and D.

All pressure data were obtained with a PSI Model 780B/T measurement system. The fully integrated instrument consisted of electronically scanned pressure transducers and a microcomputer-based data acquisition system. Individual pressure transducers provided high data acquisition rates for multiple pressure measurements. The accuracy of each transducer was maintained by frequent on-line three-point calibrations. After acquisition, information was carried by Escort, a data routing network, to a storage area for later postprocessing on Sun SPARCstations.

Inlet Flow Conditions

Inlet flow conditions were obtained from a survey of the flowfield in plane A. All reported tests were conducted with an inlet centerline Mach number of 0.6. The Reynolds number, based on the inlet diameter and centerline velocity, was 2.6×10^6. The freestream turbulence intensity, previously gathered by Reichert,[19] was nominally 0.65%. A thin turbulent inlet boundary layer existed. Representative inlet velocity profiles, plotted in nondimensional law-of-the-wall coordinates, are shown in Fig. 3. Comparisons indicated little deviation from Spalding's turbulent profile.[25] Circumferential-averaged boundary-layer parameters are listed in Table 2. δ corresponds to 95% of the freestream velocity. δ^*, θ, and H, were calculated by numerically integrating the survey data. These boundary-layer parameters were uniform around the inlet circumference.

Results and Discussion

All data presented in this article are in nondimensional form. Aerodynamic results represent mean values. Pressures are presented as total and static pressure coefficients, which are defined by Eqs. (3) and (4). The pressures p_0 and p represent local values of total and static pressure. Inlet centerline conditions define the reference states $p_{0,cl}$ and p_{cl}. Three-dimensional velocity components are presented as local Mach vectors normalized by the inlet centerline Mach number, as shown in Eq. (5):

$$Cp_0 = [(p_0 - p_{cl})/(p_{0,cl} - p_{cl})] \quad (3)$$

$$Cp = [(p - p_{cl})/(p_{0,cl} - p_{cl})] \quad (4)$$

$$M = (M/M_{cl}) \quad (5)$$

The nondimensional pressure coefficients will simply be referred to as total and static pressures. The Mach vector will be presented as streamwise and transverse velocity components. The streamwise component is perpendicular to the measurement plane, whereas the transverse component is parallel to the measurement plane. Transverse velocity components, originally on a polar grid, were interpolated onto a Cartesian mesh to enhance the interpretation of cross-stream flowfields. Since reported data were taken in only one-half of the duct, all measurement plane results have been mirror imaged for presentation.

Flow Visualization

Major flowfield characteristics were visualized with streaklines of fluorescent oil on the duct surface. Three conclusions were made from the streakline patterns. First, the near surface flow was symmetric. This was ascertained by applying different color dye to each symmetric duct half. The dye from each half remained separate and identical streakline patterns were present on each symmetric half of the duct. Second, a large region of separated flow existed, as strikingly indicated in Figs. 4 and 5. The entire duct section is shown in Fig. 4,

Table 2 Inlet boundary-layer parameters

Profile parameter	Calculated value
$(\delta/r_1) \times 100$	6.95
$(\delta^*/r_1) \times 100$	1.46
$(\theta/r_1) \times 100$	1.06
H	1.38

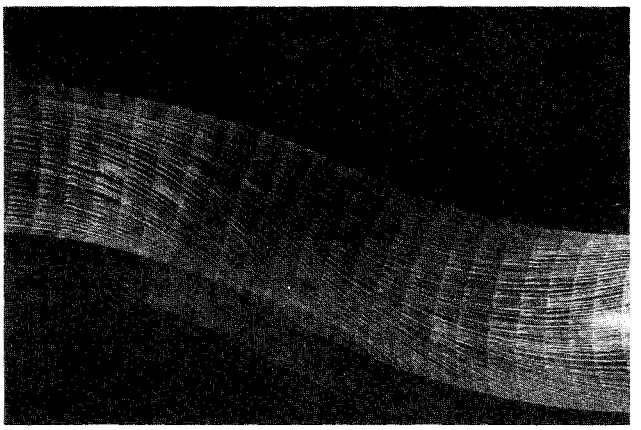

Fig. 4 Surface oil-flow patterns on one symmetric half of the duct surface.

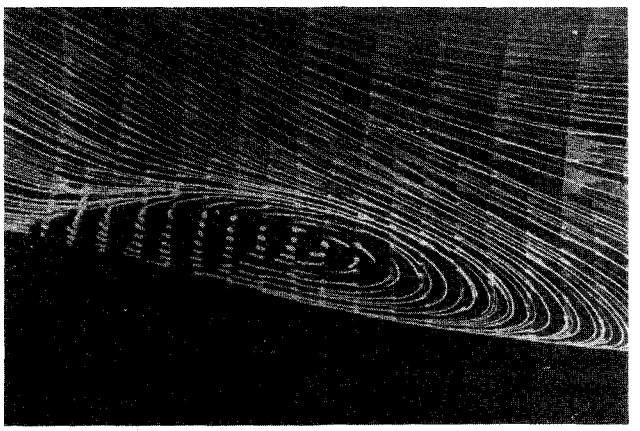

Fig. 5 Closeup of the surface oil-flow patterns near the region of separated flow.

whereas Fig. 5 is a closeup of the separated flow region. The freestream flow is from left to right, and each photograph shows only one symmetric half of the observed streakline pattern. The separation region consisted of two saddle points, occurring on the duct split line (ϕ = 180 deg), and two spiral nodes, lying on opposite sides of the duct symmetry line. The entire separated region was located on the lower duct wall. The onset of separation (upstream saddle point) was located at s/d_1 = 2.02, whereas reattachment (downstream saddle point) occurred at s/d_1 = 4.13. Third, boundary-layer cross-flows were present. In the first bend, streaklines were driven toward the lower surface (ϕ = 180 deg). In the second bend, the streaklines near ϕ = 90 deg diverged. The upper streaklines converged toward the top of the duct (ϕ = 0 deg), while the lower streaklines continued toward the bottom of the duct (ϕ = 180 deg).

A qualitative assessment of the flow in the plane of symmetry (x-z plane) was acquired by temporarily introducing a splitter plate, which divided the two symmetric duct halves. The plate was installed for only one test in order to produce streakline patterns on the plate. The S-duct surface results given above were obtained without the splitter plate in place. The splitter plane results are assumed to be qualitatively correct, even though the presence of the flat plate introduced additional shear into the flow. The streakline patterns produced on the splitter plate are presented in Fig. 6. Freestream flow is from left to right. The location of separation and reattachment are identifiable. The streaklines follow the duct curvature in the first bend. However, blockage caused by separation forced the streaklines to deviate from the curvature of the second bend. The reversed flow region began thin and appeared to grow until reattachment. The extensive bending of the streaklines at the exit of the duct was not believed to be a true feature of the flowfield when the splitter plane was not in place. Cross-stream pressure gradients at the duct exit helped drive the boundary-layer fluid on the splitter plate toward the top of the duct. This was most noticeable near the duct exit where the splitter plate boundary layer was thickest.

Surface Static Pressures

Symbols in Fig. 7 represent the static pressure variation with axial distance for three circumferential locations. The region of streamwise separated flow, deduced from flow visualization, is also shown. The effects of streamline curvature and diffusion are clearly indicated for the first bend by the pressure difference between ϕ = 10 and 170 deg and the overall pressure rise, respectively. The influence of separation is shown by the constant values of the ϕ = 90- and 170-deg static pressures between $2.0 < s/d_1 < 3.2$. The proximity of these two curves, between $2.0 < s/d_1 < 3.2$, indicate small changes in flow speed and/or direction in the lower half of the duct. The blockage, caused by the separated flow, also increased the favorable pressure gradient at ϕ = 10 deg. Static pressures at the three angles are nearly equal at s/d_1 = 2.6, suggesting that a uniform static pressure distribution exists throughout the cross-stream plane there. The static pressure rose again for $s/d_1 > 3.2$, even though the flow remained separated beyond this point, because the duct continued to diffuse. The wall static pressure distributions converged to Cp = 0.466 far downstream at s/d_1 = 8.46.

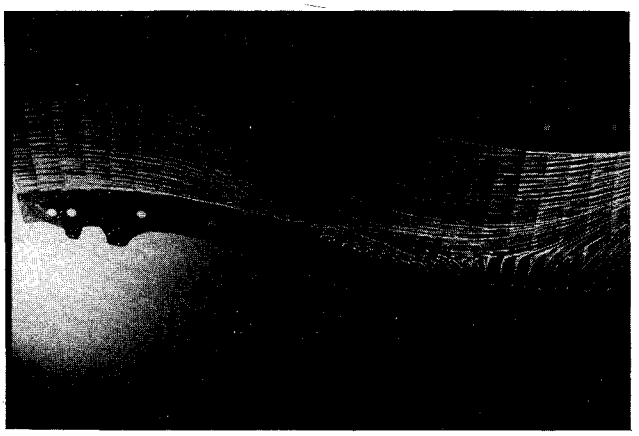

Fig. 6 Surface oil-flow patterns on the centerline splitter plate.

The circumferential distributions of surface static pressure in planes A–D are presented in Fig. 8. The pressures for plane A are nearly equal indicating no influence of the downstream duct curvature at this upstream station. The data for planes B, C, and D all reflect the presence of streamline curvature. The pressures measured in plane B are largest at ϕ = 10 deg and continually descend until ϕ = 170 deg. The actual maximum and minimum pressures in plane B most likely occurred at the top and the bottom of the duct, but were not measured because of the duct split line located there. The values at plane B are negative for $\phi > 110$ deg. Separation had not affected the flowfield at plane B yet. In planes C and D the locations of pressure maxima and minima were reversed from what they were in plane B. Measurements show that the separated flow reduced the static pressure at large values of ϕ in planes C and D.

Cross-Stream Aerodynamic Data

Contours of static pressure are shown in Fig. 9a for planes B, C, and D. The distributions in planes A and E are not presented since the measured data showed a nearly uniform cross-stream static pressure existed in those planes. The values of static pressure very near the duct surface in Fig. 9a are in excellent agreement with the data obtained from surface static pressure taps shown in Fig. 8.

Total-pressure distributions in the five planes are presented as contours in Fig. 9b. In order to help distinguish near-wall contours, expanded views of these distributions are also included for planes A and B. The convection of boundary-layer fluid away from the surface and into the core flow is quite pronounced in planes C, D, and E.

Contours of the streamwise component of velocity in all five planes are displayed in Fig. 9c. An expanded view of the inlet boundary layer is given for plane A. The distributions

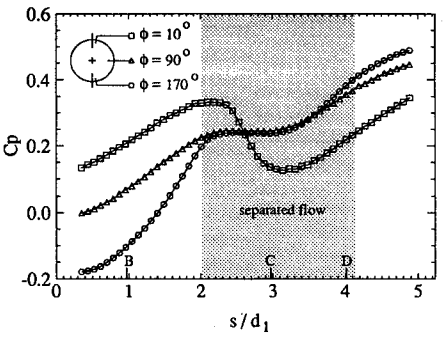

Fig. 7 Axial distributions of surface static pressures for three circumferential positions.

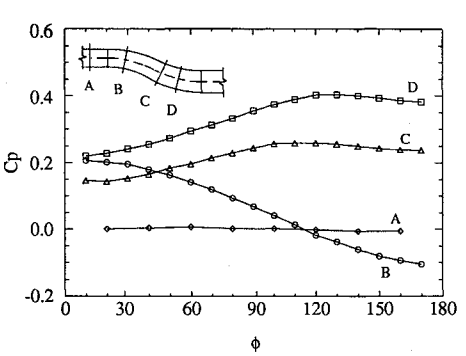

Fig. 8 Circumferential distributions of surface static pressures at four axial locations.

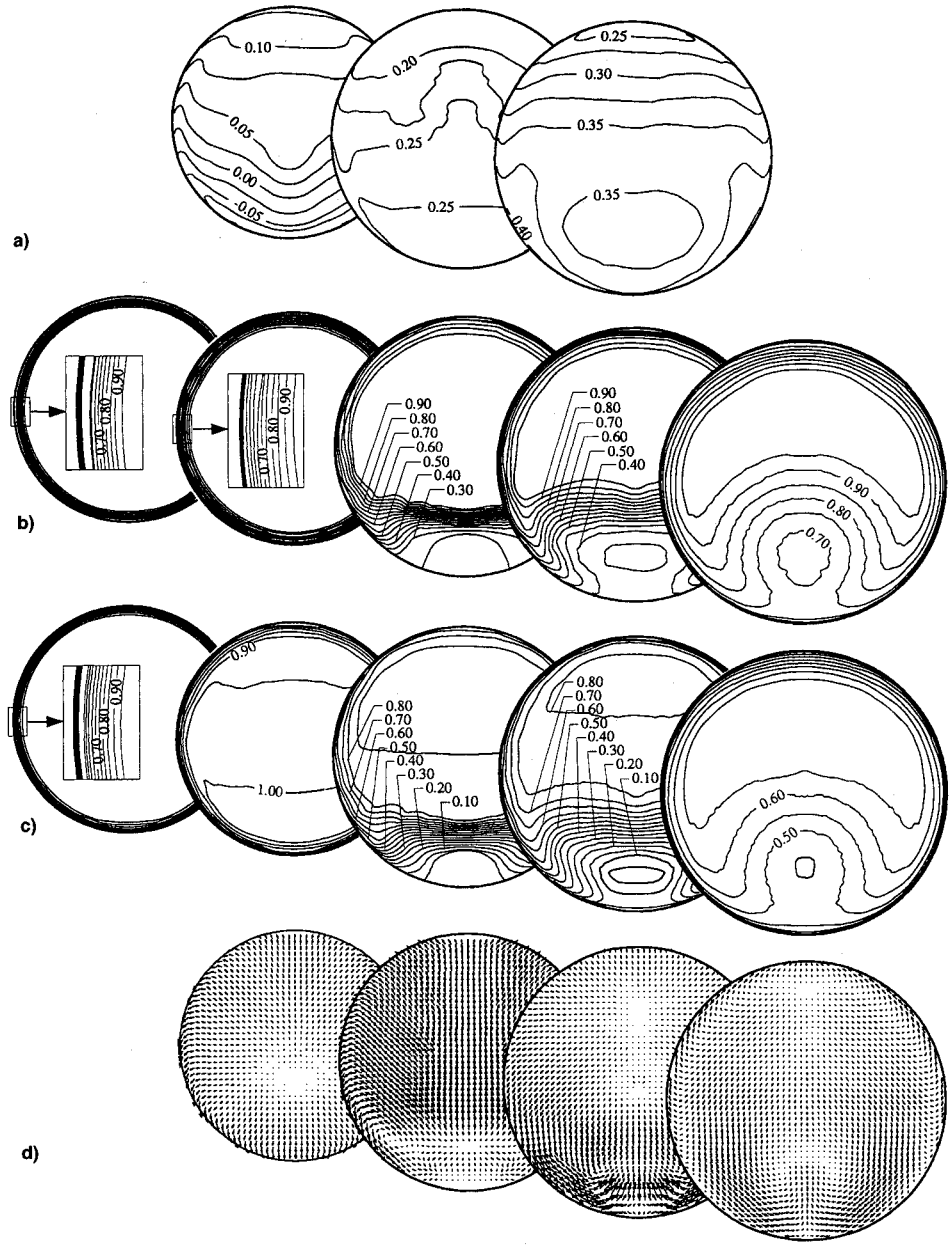

Fig. 9 Cross-stream distributions of a) static pressure, b) total pressure, c) streamwise component of velocity, and d) transverse component of velocity.

of the streamwise velocity component and total pressure are quite similar. A large region of low momentum fluid in the bottom half of the duct can again be seen within the last three planes. Planes C and D lie within the region of streamwise separated flow. Unfortunately, it was impossible to ascertain with a five-hole probe whether or not the flow was reversed at the lowest contour level of the streamwise velocity component.

Transverse velocity components are illustrated in Fig. 9d for planes B–E. Data for the plane A are not shown, since negligible crossflows (±0.3 deg) were detected there. The generation of strong crossflows within the duct can be seen. At the exit, counter-rotating vortices are present.

The flowfield at plane A corresponds to developing pipe flow. The results in Fig. 3 and Table 2 verify the boundary layer was fully turbulent. Both the total pressure and streamwise velocity contours, shown for plane A in Figs. 9b and 9c, show no circumferential variance. The measured uniform static pressure distribution in plane A corresponds well with the surface static pressure data presented previously.

Initially, the S-duct deflected the incoming flow downward. This caused the flowfield to deviate from traditional developing pipe flow by plane B. Cross-stream static pressure gradients developed. These gradients were a direct result of the core flow adjusting to duct geometry and the resulting streamline curvature. The measured static pressure distributions in plane B (Fig. 9a) indicate that the maximum static pressure existed at the top of the duct (ϕ = 0 deg), and the minimum was at the bottom of the duct (ϕ = 180 deg). These distributions are consistent with the surface static pressure data in Figs. 7 and 8.

There were two changes in the total pressure distribution from plane A to plane B. First, a slight thickening of the boundary layer occurred with downstream distance. Second, the boundary-layer thickness in plane B varied slightly with circumferential position. The boundary-layer thickness was greatest at ϕ = 0 deg and least at ϕ = 180 deg. This trend can be attributed to streamwise pressure gradients upstream of plane B which accelerated the flow near the bottom of the duct and decelerated the flow near the top of the duct. The streamwise velocity distribution in plane B also reflects the effect of streamline curvature. This can be seen in Fig. 9c, where the local Mach number exceeded the inlet Mach number near the bottom of the duct.

The transverse velocities in Fig. 9d show that crossflows occurred only near the duct surface in plane B. These crossflows were caused by cross-stream pressure gradients which turned the lower momentum fluid toward the bottom of the duct. This was also detected with flow visualization, as seen in Fig. 4. It is interesting to note that even though the pressure-driven crossflows near the duct wall were occurring in plane B, a large region of low momentum fluid was not present near the bottom of the duct. This changed by plane C.

Near the middle of the S-duct the cross-stream static pressure distribution should become nominally constant as the centerline curve undergoes an inflection. In the second bend of the duct the orientation of the cross-stream static pressure distribution should reverse, so that the lowest static pressure is near the top of the duct and the highest static pressure is near the bottom. The static pressure data for plane C in Fig. 9a verify this reversal. The data in plane C also reveal a local region of nearly constant static pressure in the lower half of the duct. This trend substantiates a previous conclusion drawn from the surface pressure data, viz., the existence of a region, in the lower half of the duct, of only small changes in flow speed and/or direction. It is also consistent with the streamwise separated flow there.

Strong crossflows existed near the lower duct surface in plane C (Fig. 9d). The crossflows suggest that two vortical structures were developing. These vortices were not present in plane B. The crossflows continually moved boundary-layer fluid into the low velocity region. The accumulation of low momentum fluid in the bottom portion of plane C can be discerned in the total pressure and streamwise velocity data. This accumulation was not only caused by the convection of boundary-layer fluid toward the lower surface, but also by the reversed flow and the adverse streamwise pressure gradient upstream of plane C.

A significant amount of upward deflected flow at the centerline in plane C is shown in Fig. 9d. This confirms the results obtained from the surface flow visualization on the temporary centerline splitter plane. This deflection was a direct consequence of two factors: 1) blockage created by flow separation and 2) crossflows driven by pressure gradients.

The static pressure data in plane D are similar to static pressure data in plane C. The measured distribution still indicated a substantial region of nearly constant static pressure in the lower half of the duct ($Cp \approx 0.35$). This region was also present in plane C. It must be noted, however, that the static pressure distribution in plane D, which was further from the middle of the duct, varied more than the distribution in plane C.

Total pressures and streamwise velocities suggest further growth of the low total pressure/low velocity region in the bottom half of the duct. Measurements indicate that enough low momentum fluid was carried away from the duct wall to form a region of near zero streamwise velocity, far from the surface.

Strong crossflows still existed near the lower duct surface in plane D. These crossflows continually drove boundary-layer fluid toward the low-velocity region. A strong vortical structure developed. For the aerodynamic measurements, the core flow returned to the nominal streamwise direction by the time it reached plane D. This is contrary to the splitter plate streakline patterns. This inconsistency was caused by the pressure gradients that drove the boundary-layer fluid on the splitter plate toward the top of the duct, as previously explained. Transverse velocity plots also revealed that the boundary-layer fluid at the top of the duct began to turn upward. This reversal in cross-stream flow direction was caused by the change in static pressure distribution from plane B to plane D. It is interesting to note that even though plane D is well into the second bend, no large vortical structure existed at the top of the duct in plane D.

By plane E the freestream flow returned nominally to the x direction. Cross-stream static pressure gradients were nearly eliminated, and are therefore not illustrated. Even though cross-stream static pressure gradients were weak in plane E, upstream of plane E, pressure gradients were strong enough to fully reverse the direction of the boundary-layer fluid flow on the upper surface of the duct, as seen in Fig. 9d. This was also detected with flow visualization. This phenomenon had just begun in plane D.

A pair of counter-rotating vortices, located in the lower half of the duct, had completely evolved by plane E. These vortices now convected the low momentum fluid of the boundary layer toward the center of the duct. Low momentum fluid convection by the vortices degraded both the uniformity and magnitude of the exit total pressure distribution. The measured region of low momentum fluid in plane E extended above the duct centerline. This trend had been observed before by previous investigators.[4,8] The inability of numerical algorithms to capture this flow phenomenon has also been documented by several researchers.[12,14,15]

Summary

The flow through the S-duct evolved from a strong interaction between the boundary layer and the core flow. Results show the flow was symmetric about the x-z plane. A large region of streamwise flow separation occurred within the duct. Duct curvature induced strong pressure-driven secondary flows, which evolved into a large pair of counter-rotating vortices. These vortices convected the low momentum fluid of the boundary layer toward the center of the duct, degrading both the uniformity and magnitude of the total pressure profile. The benchmark data collected should be beneficial to inlet designers and is suitable for code validation.

Acknowledgments

The authors express their appreciation to NASA Lewis Research Center, Cleveland, Ohio, who sponsored this work under Grant NAG 3-1275. In addition, the authors would like to acknowledge the personnel without whose support this research endeavor would not have been possible. In particular the authors would like to thank R. Davis, K. Hall, W. Darby, M. Peters, B. Wendt, and W. Hingst for their advice, support, and assistance.

References

[1]Bauermeister, W. K., Roseburg, C. M., and Ip, H. W., "727 Airplane Engine Inlet Development," AIAA Paper 68-595, June 1968.

[2]Little, B. H., and Trimboli, W. S., "An Experimental Investigation of S-Duct Diffusers for High-Speed Prop-Fans," AIAA Paper 82-1123, June 1982.

[3]Rowe, M., "Measurements and Computations of Flow in a Pipe Bend," *Journal of Fluid Mechanics*, Vol. 43, Pt. 4, 1970, pp. 771–783.

[4]Bansod, P., and Bradshaw, P., "The Flow in S-Shaped Ducts," *Aeronautical Quarterly*, Vol. 23, May 1972, pp. 131–140.

[5]Sullivan, J. P., Murthy, S. N. B., Lan, T. H., Davis, R., and Hong, S., "S-Shaped Duct Flows," Purdue Univ. School of Aeronautics and Astronautics Rept. S-ONR-TSR-80-2, West Lafayette, IN, Oct. 1980.

[6]Guo, R. W., and Seddon, J., "The Investigations of Swirl in an S-duct," *Aeronautical Quarterly*, Vol. 33, May 1982, pp. 25–58.

[7]Taylor, A. M. K. P., Whitelaw, J. H., and Yianneskis, M., "Developing Flow in S-Shaped Ducts II—Circular Cross-Section Duct," Imperial Valley College of Science and Technology NASA CR 3759, Imperial, CA, Feb. 1984.

[8]Vakili, A. D., Wu, J. M., Liver, P., and Bhat, M. K., "Experimental Investigation of Secondary Flows in a Diffusing S-Duct," Univ. of Tennessee Space Inst. Preliminary Copy Final Rept. for NASA Contract NAG3 233, Nashville, TN, Sept. 1984.

[9]Taylor, A. M. K. P., Whitelaw, J. H., and Yianneskis, M., "Developing Flow in S-Shaped Ducts I—Square Cross-Section Duct," Imperial Valley College of Science and Technology NASA CR 3550, Imperial, CA, 1982.

[10]Taylor, A. M. K. P., Whitelaw, J. H., and Yianneskis, M., "Curved

Ducts with Strong Secondary Motion: Velocity Measurements of Developing Laminar and Turbulent Flow," *Journal of Fluids Engineering*, Vol. 104, Sept. 1982, pp. 350–359.

[11]Sullivan, J. P., Murthy, S. N. B., Davis, R., and Hong, S., "S-Shaped Duct Flows," Office of Naval Research Contract N-78-C-0710, Purdue, IN, Dec. 1982.

[12]Harloff, G. J., Reichert, B. A., and Wellborn, S. R., "Navier-Stokes Analysis and Experimental Data Comparison of Compressible Flow in a Diffusing S-Duct," AIAA Paper 92-2699, June 1992; also NASA TM 105683, July 1992.

[13]Harloff, G. J., Smith, C. F., Bruns, J. E., and DeBonis, J. R., "Navier-Stokes Analysis of Three-Dimensional S-Ducts," *Journal of Aircraft*, Vol. 30, No. 4, 1993, pp. 526–533.

[14]Smith, C. F., Bruns, J. E., Harloff, G. J., and Debonis, J. R., "Three-Dimensional Compressible Turbulent Computations for a Diffusing S-Duct," Sverdrup Technology, NASA CR 4392, Cleveland, OH, 1991.

[15]Towne, C. E., and Anderson, B. H., "Numerical Simulation of Flows in Curved Diffusers with Cross-Sectional Transitioning Using a Three-Dimensional Viscous Analysis," NASA TM 81672, Jan. 1981.

[16]Towne, C. E., "Computation of Viscous Flow in Curved Ducts and Comparison with Experimental Data," AIAA Paper 84-0531, Jan. 1984.

[17]Vakili, A., Wu, J. M., Hingst, W. R., and Towne, C. E., "Comparison of Experimental and Computational Compressible Flow in a S-Duct," AIAA Paper 84-0033, Jan. 1984.

[18]Povinelli, L. A., and Towne, C. E., "Viscous Analysis of Flow Through Subsonic and Supersonic Intakes," NASA TM 88831, Sept. 1986.

[19]Reichert, B. A., Hingst, W. R., and Okiishi, T. H., "An Experimental Comparison of Nonswirling and Swirling Flow in a Circular-to-Rectangular Transition Duct," AIAA Paper 91-0342, Jan. 1991; also NASA TM 104359, Jan. 1991.

[20]Sirbaugh, J. R., and Reichert, B. A., "Computation of a Circular-to-Rectangular Transition Duct Flow Field," AIAA Paper 91-1741, June 1991.

[21]Porro, A. R., Hingst, W. R., Wasserbauer, C. A., and Andrews, T. B., "The NASA Lewis Research Center Internal Fluid Mechanics Facility," NASA TM 105187, Sept. 1991.

[22]Wellborn, S. R., "A Study of the Compressible Flow Through a Diffusing S-Duct," M.S. Thesis, Iowa State Univ., Ames, IA, 1993.

[23]Wendt, B. J., and Reichert, B. A., "A New Algorithm for Five-Hole Probe Calibration and Data Reduction and its Application to a Rake-Type Probe," American Society of Mechanical Engineers Paper FED-Vol. 161, June 1993.

[24]Reichert, B. A., and Wendt, B. J., "A New Algorithm for Five-Hole Probe Calibration, Data Reduction and Uncertainty Analysis," NASA TM 106458, March 1994.

[25]White, F. M., *Viscous Fluid Flow*, McGraw-Hill, New York, 1991.

Recommended Reading from Progress in Astronautics and Aeronautics

Numerical Approaches to Combustion Modeling

Edited by
Elaine S. Oran and Jay P. Boris
Naval Research Laboratory

Drawing on the expertise of leading researchers in the field of combustion modeling, this unique book illustrates how to construct, use, and interpret numerical simulations of chemically reactive combustion flows. The text is written for scientists, engineers, applied mathematicians, and advanced students.

Subjects ranging from fundamental chemistry and physics to very applied engineering applications are presented in 24 chapters in four parts: Chemistry in Combustion Modeling; Flames and Flames Structure; High-Speed Reacting Flows; (Even More) Complex Combustion Systems. Includes more than 1400 references, 345 tables and figures, 900 equations, and 12 color plates.

1991, 900 pp, illus, Hardback, ISBN 1-56347-004-7,
AIAA Members $89.95, Nonmembers $109.95,
Order #: V-135 (830)

Place your order today! Call 1-800/682-AIAA

AIAA
American Institute of Aeronautics and Astronautics

Publications Customer Service, 9 Jay Gould Ct., P.O. Box 753, Waldorf, MD 20604
FAX 301/843-0159 Phone 1-800/682-2422 8 a.m. - 5 p.m. Eastern

Sales Tax: CA residents, 8.25%; DC, 6%. For shipping and handling add $4.75 for 1-4 books (call for rates for higher quantities). Orders under $100.00 must be prepaid. Foreign orders must be prepaid and include a $20.00 postal surcharge. Please allow 4 weeks for delivery. Prices are subject to change without notice. Returns will be accepted within 30 days. Non-U.S. residents are responsible for payment of any taxes required by their government.